Appl. Phys. B 72, 823–833 (2001) / Digital Object Identifier (DOI) 10.1007/s003400100538

Applied Physics B
Lasers
and Optics

Kinetic modelling of a discharge-pumped ArF excimer laser and the effects of discharge filamentation

A.V. Demyanov[1], **L. Feenstra**[2], **P.J.M. Peters**[3,*], **A.P. Napartovich**[1], **W.J. Witteman**[3]

[1] Troitsk Institute of Innovative and Thermonuclear Research (TRINITI), Troitsk 142092, Moscow Province, Russia
(E-mail: apn@triniti.ru)
[2] Laser Centre Vrije Universiteit, Department of Physics and Astronomy, De Boelelaan 1081, 1081 HV Amsterdam, The Netherlands
[3] University of Twente, Faculty of Applied Physics, Quantum Electronics Group, P.O. Box 217, 7500 AE Enschede, The Netherlands

Received: 23 August 2000/Revised version: 6 December 2000/Published online: 27 April 2001 – © Springer-Verlag 2001

Abstract. Results of kinetic modelling of an X-ray preionised, discharge-pumped ArF excimer laser, operating with a spiker-sustainer circuit are presented. The parallel-resistor model includes the complete ArF laser kinetics and calculations of the Boltzmann equation in each layer taking into account the effects of electron–electron and super-elastic collisions. The model further includes a detailed description of the electrical circuit and the formation of filaments with a realistic electrode profile. This model shows a good correspondence with the experimental results in predicting laser energy and optical behaviour. Neglecting the formation of filaments and the electron–electron and super-elastic collision processes yields remarkably poorer results. Parametric studies on the electrode profile, the formation of micro-arcs and on the electrical circuit parameters were performed numerically.

PACS: 42.55.Lt; 52.65.-y; 52.80.Hc; 42.60.By

Recently, interest in the electric-discharge-excited ArF laser ($\lambda = 193$ nm) has grown strongly, due to its application possibilities in medicine and lithography. The processes taking place in the active medium of this laser were studied experimentally [1–9] and theoretically [10–13]. The number densities of electrons, of negative fluorine ions and of several excited species were measured in [1–3], respectively. The optimisation of the gas mixture composition, the electrode construction, the electrical circuit and the application of a gas cleaning system yielded a laser efficiency of up to 2.1% [4], laser pulse energies of up to 550 mJ [5], pulse lengths of up to 120 ns [6] and increased gas-mixture life times of up to 10^9 pulses in one month [7–9].

Numerically, the upper energy limit for a typical ArF laser pulse, as imposed by the development of micro-channels, was evaluated in the frame of a zero-dimensional model and for an idealised electric circuit [10]. A one-dimensional fluid model was described in [11, 12], to study the formation of cathode and anode layers and to investigate the effects of gas photo-ionisation. The same authors have developed a two-dimensional fluid model [13], which includes solving of the continuity equations, the Poisson equation and the electric-circuit equations. This model was applied for the study of the formation of a micro-arc initiated by a protrusion on the cathode surface or a non-uniform heating of the gas by a preceding discharge pulse. It was found that the level of preionisation electron density controls the evolution of micro-arcs, even suppressing them at high electron densities. It should be noted that almost all known mechanisms for plasma instabilities are ignored in this model [13] due to a very simplified ionisation balance description.

For a number of applications longer laser pulses are desirable. However, the laser pulse length does not increase beyond a certain value when the pumping pulse is extended, e.g. by using a pulse-forming network. The discharge pulse can get significantly longer than the laser pulse. A plausible explanation is that micro-arcs, seen on photos of the discharge, terminate lasing, because of spoiling the optical quality of the medium [14] or because of an energy redistribution between the bulk of the plasma and the micro-arcs [15]. Both effects become important at a high electron number density. However, the dependence of micro-arc-induced optical losses on the filament parameters is not known. The formation of filaments is controlled by plasma instabilities and can be provoked by hot spots appearing at the electrode surface [14]. Concerning the role of a precursor for a filament, one can argue that starting from a hot spot a streamer will result in formation of the filament only when it propagates in an unstable plasma. The development of instabilities involves many processes that influence the ionisation balance and therefore are very sensitive to the gas composition and plasma characteristics like the electron and excited atoms number densities, which in turn depend on the local electrical field and the electron energy distribution function (EEDF). A numerical model that is able to predict an instability, should describe correctly the plasma background just before the development of the instability. This is a reason why the numerical model should be as complete as possible. On the other side it is important, that the model includes spatial non-uniformities of the plasma density and the electrical

*Corresponding author.
(Fax: +31-53/489-1102, E-mail: p.j.m.peters@tn.utwente.nl)

field strength. A simple way to describe spatial gradients in a plasma associated with an initial non-uniform degree of ionisation or caused by a special shape of the electrodes is the so-called parallel-resistor model (PRM) [16]. From the above discussion it follows that combining the full kinetic model with the PRM is the most reliable way to achieve an adequate description of real experimental devices. One more important issue is the necessity to describe correctly the electrical circuit employed in experiments. Formation of short electrical pulses requires a particular care in preparation, the electrical circuit resulting in a complex and not well characterised structure. The authors are not aware of any theoretical model for a discharge-pumped ArF laser satisfying the requirements discussed above.

Some of the above-discussed problems were studied while modelling XeCl and KrF excimer lasers [16–23]. In this paper the achievements obtained in the previous papers are taken into account in our formulation of the parallel-resistor model which includes filaments. The resulting model is used for the description of experiments on a discharge-pumped ArF laser using a gas mixture of $F_2 : Ar : He = 0.06 : 5.00 : 94.94$ at 5 bar total pressure. A description of the experimental setup and experimental results are presented in Sect. 1. The numerical model and the simulation results together with a comparison between the simulation results and the experiments are described in Sects. 2 and 3. In Sect. 4 the influence of a number of parameters on the calculated results is discussed, particularly the sensitivity of the laser pulse shape and energy to variations in the electric circuit parameters, the electrode shape and some kinetic processes. Conclusions are summarised in Sect. 5.

1 Experimental set-up and results of measurements

The laser head is a rectangular stainless-steel vessel, see Fig. 1, fitted with uncoated MgF_2 windows. The resonator mirrors, a 10-m concave-radius full reflector and a 70% reflecting plane outcoupler, are placed outside the vessel. The brass laser cathode is of Ernst's uniform field type, with $k_0 = 0.04$ [24]. The nickel-plated aluminium anode is flat. The total discharge volume is approximately $60 \times 0.7 \times 1.2\,\mathrm{cm}^3$ $(l \times w \times h)$. The peaking capacitors are placed close to the laser electrodes, inside the laser vessel, to minimise the self-inductance of the spiker circuit.

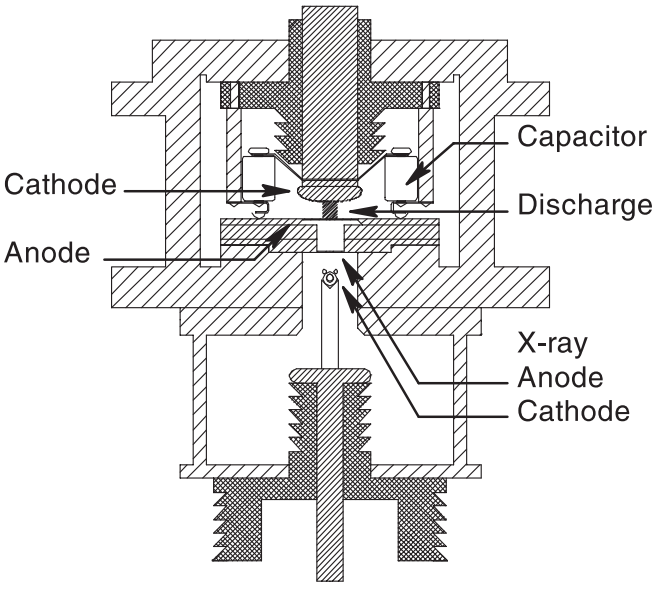

Fig. 1. The laser head with the X-ray source. The discharge volume is preionised through the laser anode. The peaking capacitors are mounted inside the laser vessel to minimise the self-inductance

To decrease the self-inductance of the main circuit, aluminum short-circuiting rods are placed in the laser vessel, as well.

The discharge area is preionised with X-rays through the 1-mm-thick laser anode. The X-ray source uses a corona-plasma cathode [25, 26], the anode is a 20-μm tungsten coating on the 1-mm thick aluminium pressure window between the X-ray source and the laser vessel, see Fig. 1. The X-ray pulse of 50 ns (FWHM) produces approximately 1.75×10^9 electrons/cm^3 in the laser gas mixture. To measure the electron density we used the electrodes inside the laser chamber as a charge collector. The laser electrodes are incorporated in a current loop with a storage capacitor and a measuring resistor [26].

The laser gas is electrically excited with a spiker-sustainer circuit with a multi-channel rail gap (RG) separating the pulse forming network (PFN) from the laser head and the peaking capacitors C_P, see Fig. 2. The electrical circuit operates in the so-called swing mode [27, 28]. This means that a fast, high-voltage prepulse of opposite polarity to the PFN voltage is applied to the peaking capacitors at the moment the PFN ca-

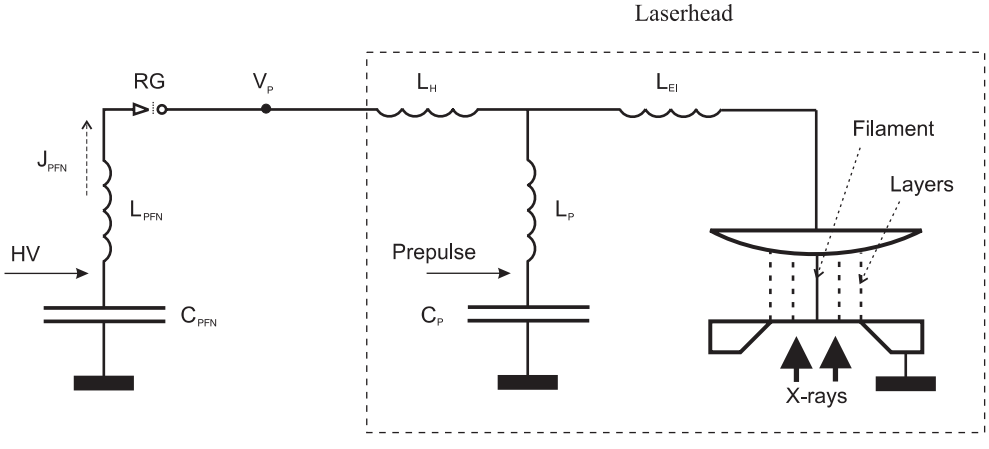

Fig. 2. Equivalent electrical circuit of model and discharge geometry. C_{PFN}, pulse-forming network (PFN); C_P, peaking capacitor; HV, PFN charging circuit. Prepulse: prepulse generator. $C_{PFN} = 140$ nF, $C_P = 4.6$ nF, $L_{PFN} = 8$ nH, $L_H = 15$ nH, $L_P = 2.4$ nH, $L_{EL} = 1$ nH

pacitor C_{PFN} has been fully charged. The prepulse causes the rail gap to break down, thus allowing a current to flow from the large C_{PFN} to the small peaking capacitors, resulting in a high voltage overswing on the peaking capacitors. This voltage spike will start the laser discharge, which is subsequently sustained by the current from the PFN.

The laser gas mixture composition is $F_2 : Ar : He = 0.06 : 5.00 : 94.94$ at 5 bar total pressure. The capacitances are: $C_{PFN} = 164$ nF, $C_P = 4.6$ nF and typical operating voltages are $V_{PP} = 30$ kV and $V_{PFN} = 32$ kV. Typical values for the optical pulse are $E_{OUT} = 90$ mJ in a laser pulse of 25 ns (FWHM).

The temporal behaviour of the voltage and the current are measured outside the laser vessel with resistive probes (the points where the current J_{PFN} and voltage V_P were measured are indicated in Fig. 2). Thus the actual discharge voltage and current are not measured. The optical pulse is monitored by a filtered photodiode and the output energy is measured with a GenTec pyroelectric energy meter. The beam size is determined by its imprint on thermofax paper and is equal to 0.7×1.2 cm^2.

2 Theoretical model

The theoretical model developed describes large spatial-scale non-uniformities (LSSN) (as introduced by Kushner [17]) in the layers of the parallel-resistor model (PRM), and small-scale non-uniformities (filaments) induced by local electric field disturbances in a fixed total area. The full kinetic model includes solving of the electron Boltzmann equation in parallel with the kinetic equations for a large number of neutral and charged species in each layer. Electron–electron collisions and second-kind collisions are properly accounted for when calculating the EEDF. A short-pulse electric circuit was modelled and incorporated in the model.

2.1 Parallel-resistor model (PRM)

Since the field inhomogeneities caused by the profiling of the electrode are typically of ~ 1 cm scale, at high gas pressure of a few bar, diffusion fluxes can be neglected. The plasma volume between the electrodes was sectioned into layers, parallel to the optical axis and electrical current. All plasma parameters were assumed to be uniform within every layer, and exchange of particles and energy between the layers was neglected. On the other hand a LSSN, induced by the electrode profile is described correctly when the number of layers is high enough. In our calculations the number of layers was taken to be 20. Special test simulations with an increased number of layers demonstrated minor changes in the final results. The preionisation electron density profile can be varied as well. The applied voltage and the electrode profile define the electric field strength in each layer. The electric field decreases from the axis to the edges of the electrodes, corresponding to the increase of the inter-electrode distance from the axis outward (see also Fig. 2). The total discharge current, which is used to calculate the discharge voltage from the electrical circuit equations, is the sum of all electrical currents in each layer. The electrical field strength E/N which is used in the Boltzmann solver, in each discharge layer is determined by the discharge voltage and the electrode separation, where as usual for high-pressure discharges the cathode fall has been neglected. Using the terminology of Kushner [17], the approach described above is appropriate for the analysis of the dynamics of the LSSN. This was used in [18–22] to study the dynamics of the transverse plasma profile in a XeCl laser and in [17] to evaluate the effect of the misalignment of plane electrodes in a KrF laser. In contrast to [17], both the parallel-resistor model and the real shape of the electrode profiles as used in the experiments were taken into account in this work. The results of our simulations, reported below, demonstrate the importance of the correct description of this property.

2.2 Filament formation

As discussed in the introduction, the most probable mechanism for the early termination of the laser pulse is the formation of micro-arcs or filaments (see also a detailed discussion of this mechanism for a KrF laser in [17]). To evaluate this effect we introduced in the model an additional layer located along the discharge axis, where the electrical field has a maximum (see Fig. 2). In this layer the same set of equations, except the photon equation, was also solved as in the other layers. The area of this layer is formed by the total cross-section of all micro-arcs. In our simulations the total area of all filaments was estimated by taking the number of filaments from the experiment (the observed period between the filaments was 1–2 mm) and the estimated filament diameter was 100–200 μm using the results of 2-D simulations of micro-arcs in an ArF laser [13]. Despite some differences in the composition of the laser gas mixture (in [13] it was $F_2 : Ar : He = 0.24 : 7.89 : 91.87$ at a total pressure of 2.53 bar), one may hope that this estimate is correct with respect to the order of magnitude. As a result, the value of the total filament area was taken to be 1.1 cm^2 in our simulations. This corresponds to $\sim 2.6\%$ of the total discharge area. The total current in the electric circuit was composed of the currents through all layers and through the filament area. It should be noted that laser gain is produced only in the layers.

It was shown [21] that the development of micro-arcs is much more sensitive to a perturbation of the electrical field than to a fluctuation of the preionisation level. Taking into account that in the experiment X-ray preionisation was used providing a quite good plasma homogeneity, it was assumed that the electric field strength in the filament is proportional to the electric field at the centre of the plasma layer, with a proportionality factor which is varied in the calculations. In other words, $|E_0 - E_f| = \kappa E_0$, where the magnitude of κ is estimated to reflect the appearance of hot spots at the cathode. Evidently, this is an assumption. The second physically reasonable option is to assume that an increment of electric field in the filament may be found from the discharge voltage accounting for a lower cathode fall at this place. (It should be recalled that the cathode fall is usually neglected in numerical simulations.) Test calculations demonstrated that between results obtained for both options the difference is not significant. The disturbance of the electric field within the filament κ, was estimated from a decrement of the cathode voltage fall of 70 V which is a reasonable value for the cathode voltage reduction produced by hot spot formation.

This approach is a simplified version of Kushner's more rigorous filament treatment in [17]. In particular, we replace

the realistic profile of the parameters within a filament by a stepwise one and we neglect the effects of the gas-dynamic expansion. Nevertheless we use a rather complete kinetic description with real electrode profiles and study the effect of a local voltage disturbance.

2.3 The electric circuit

A correct simulation of the electric circuit used in the experiments is not a trivial problem. A rigorous simulation of the PFN would require the use of a model with distributed parameters. In Fig. 2, a simplified model of the used electrical circuit is given. Keeping essential features of the circuit, we have replaced the PFN by a self-inductance L_{PFN} and capacitance C_{PFN} with appropriate values. It should be noticed that the laser-head stray inductance makes this approximation more applicable by smoothing the pumping pulse. The calculations start at the moment the voltage at the peaking capacitor is at its maximum value but at opposite polarity to the voltage on the PFN. In the experiments (see above) the voltage and the current are measured on top of the laser vessel and not on the electrodes. For comparison with the experimental results, the current from the PFN and the voltage were calculated at the point V_{P} of the equivalent electric circuit in Fig. 2. The equivalent circuit also includes the inductance of the laser head L_{H}, and the inductance of the peaking capacitors and of the connectors L_{P}. As can be seen from Fig. 1, the peaking capacitors are connected to the upper part of the electrode. The area between the connection point of the peaking capacitors and the plasma possesses a small additional inductance L_{EL}. None of the mentioned inductances were measured and they served as fitting parameters to provide the best agreement between the calculated and measured waveforms of the PFN current and voltage V_{P}.

2.4 Kinetic reactions and Boltzmann solver

The list of processes that are included in the kinetic model is given in Table 1. Data for reaction rate coefficients are taken

Table 1. List of processes included in the model

Reaction	Rate (10^{X}) cm^3/s, cm^6/s, s^{-1}	Reference
$\mathrm{Ar}+\mathrm{e}\rightarrow \mathrm{Ar}^+ +\mathrm{e}+\mathrm{e}$	Boltzmann equation (BE)	
$\mathrm{Ar}+\mathrm{e}\rightarrow \mathrm{Ar}^* +\mathrm{e}$	BE	
$\mathrm{Ar}+\mathrm{e}\rightarrow \mathrm{Ar}^{**} +\mathrm{e}$	BE	
$\mathrm{Ar}^* +\mathrm{e}\rightarrow \mathrm{Ar}^{**} +\mathrm{e}$	BE	
$\mathrm{Ar}^* +\mathrm{e}\rightarrow \mathrm{Ar}^+ +\mathrm{e}+\mathrm{e}$	BE	
$\mathrm{Ar}^{**} +\mathrm{e}\rightarrow \mathrm{Ar}^+ +\mathrm{e}+\mathrm{e}$	BE	
$\mathrm{Ar}_2^+ +\mathrm{e}\rightarrow \mathrm{Ar}^{**} +\mathrm{Ar}$	BE	
$\mathrm{F}_2+\mathrm{e}\rightarrow \mathrm{F}^- +\mathrm{F}$	BE	
$\mathrm{F}_2(\mathrm{Vib})+\mathrm{e}\rightarrow \mathrm{F}^- +\mathrm{F}$	BE	
$\mathrm{F}_2+\mathrm{e}\rightarrow \mathrm{F}_2(\mathrm{Vib})+\mathrm{e}$	BE	
$\mathrm{He}+\mathrm{e}\rightarrow \mathrm{He}^+ +\mathrm{e}+\mathrm{e}$	BE	
$\mathrm{He}+\mathrm{e}\rightarrow \mathrm{He}^* +\mathrm{e}$	BE	
$\mathrm{He}+\mathrm{e}\rightarrow \mathrm{He}^{**} +\mathrm{e}$	BE	
$\mathrm{He}^* +\mathrm{e}\rightarrow \mathrm{He}^{**} +\mathrm{e}$	BE	
$\mathrm{He}^* +\mathrm{e}\rightarrow \mathrm{He}^+ +\mathrm{e}+\mathrm{e}$	BE	
$\mathrm{He}^{**} +\mathrm{e}\rightarrow \mathrm{He}^+ +\mathrm{e}+\mathrm{e}$	BE	
$\mathrm{He}_2^+ +\mathrm{e}\rightarrow \mathrm{He}^{**} +\mathrm{He}$	BE	
$\mathrm{He}^+ +\mathrm{He}+\mathrm{He}\rightarrow \mathrm{He}_2^+ +\mathrm{He}$	1.0(−31)	[28]
$\mathrm{Ar}^+ +\mathrm{Ar}+\mathrm{Ar}\rightarrow \mathrm{Ar}_2^+ +\mathrm{Ar}$	2.5(−31)	[29]
$\mathrm{Ar}^+ +\mathrm{Ar}+\mathrm{He}\rightarrow \mathrm{Ar}_2^+ +\mathrm{He}$	1.0(−32)	[30]
$\mathrm{Ar}^* +\mathrm{F}_2\rightarrow \mathrm{ArF}^* +\mathrm{F}$	4.0(−10)	[31]
$\mathrm{Ar}^+ +\mathrm{F}^-\rightarrow \mathrm{ArF}^*$	9.1(−7)	[32]
$\mathrm{Ar}_2^+ +\mathrm{F}^-\rightarrow \mathrm{ArF}^* +\mathrm{Ar}$	9.26(−7)	[32]
$\mathrm{He}^+ +\mathrm{F}^-\rightarrow \mathrm{F}^* +\mathrm{He}$	6.94(−6)	[32]
$\mathrm{He}_2^+ +\mathrm{F}^-\rightarrow \mathrm{F}^* +\mathrm{He}+\mathrm{He}$	5.08(−6)	[32]
$\mathrm{Ar}^{**}\rightarrow \mathrm{Ar}^* +\mathrm{Phot}$	1.4(+7)	[33]
$\mathrm{He}^{**}\rightarrow \mathrm{He}^* +\mathrm{Phot}$	1.0(+8)	Estimate
$\mathrm{ArF}^*\rightarrow \mathrm{Ar}+\mathrm{F}+h\nu$	2.38(+8)	[34]
$\mathrm{ArF}^* +\mathrm{Rad}\rightarrow \mathrm{Ar}+\mathrm{F}+\mathrm{Rad}$	2.7(−16)	[34]
$\mathrm{Ar}^{**} +\mathrm{Rad}\rightarrow \mathrm{Ar}^+ +\mathrm{e}$	3.0(−18)	[2]
$\mathrm{F}_2+\mathrm{Rad}\rightarrow \mathrm{F}+\mathrm{F}$	1.5(−21)	[2]
$\mathrm{F}^- +\mathrm{Rad}\rightarrow \mathrm{F}+\mathrm{e}$	9.7(−18)	[10]
$\mathrm{Ar}_2\mathrm{F}^* +\mathrm{Rad}\rightarrow \mathrm{ArF}^* +\mathrm{Ar}$	1.0(−18)	[35]
$\mathrm{Ar}_2^* +\mathrm{Rad}\rightarrow \mathrm{Ar}_2^+ +\mathrm{e}$	4.0(−18)	[10]
$\mathrm{ArF}^* +\mathrm{e}\rightarrow \mathrm{Ar}+\mathrm{F}+\mathrm{e}$	2.0(−7)	[10]
$\mathrm{ArF}^* +\mathrm{F}_2\rightarrow \mathrm{Ar}+\mathrm{F}+\mathrm{F}+\mathrm{F}$	1.900(−9)	[10]
$\mathrm{ArF}^* +\mathrm{Ar}\rightarrow \mathrm{Ar}+\mathrm{Ar}+\mathrm{F}$	9.000(−12)	[10]
$\mathrm{ArF}^* +\mathrm{He}\rightarrow \mathrm{He}+\mathrm{Ar}+\mathrm{F}$	1.000(−12)	[35]
$\mathrm{ArF}^* +\mathrm{He}+\mathrm{Ar}\rightarrow \mathrm{Ar}_2\mathrm{F}^* +\mathrm{He}$	1.000(−31)	[35]
$\mathrm{Ar}^* +\mathrm{Ar}^*\rightarrow \mathrm{Ar}^+ +\mathrm{e}+\mathrm{Ar}$	5.000(−10)	[10]
$\mathrm{Ar}_2\mathrm{F}^* +\mathrm{He}\rightarrow \mathrm{Ar}+\mathrm{Ar}+\mathrm{F}+\mathrm{He}$	1.000(−12)	[10]
$\mathrm{Ar}^* +\mathrm{Ar}+\mathrm{Ar}\rightarrow \mathrm{Ar}_2^* +\mathrm{Ar}$	2.500(−32)	[36]
$\mathrm{Ar}^* +\mathrm{Ar}+\mathrm{He}\rightarrow \mathrm{Ar}_2^* +\mathrm{He}$	8.000(−33)	Estimate
$\mathrm{Ar}_2^*\rightarrow \mathrm{Ar}+\mathrm{Ar}$	2.380(+8)	[36]
$\mathrm{F}^*\rightarrow \mathrm{F}+\mathrm{Phot}$	2.700(+8)	Estimate

from [10, 29–36]. The electron scattering cross sections are taken from [37–41]. The steady-state Boltzmann equation for the electron energy distribution function (EEDF) was solved in a two-term approximation; electron–electron collisions and second-kind collisions were taken into account, as well. The local field approximation for the Boltzmann equation used in this model is valid when the voltage rise time is longer than the electron energy relaxation time and when the thickness or radius of a micro-arc is greater than the energy relaxation length. For the considered experimental condition the energy relaxation time and length are equal to about 0.5 ns and 5 μm, respectively. It should be remembered that the kinetic equations and the Boltzmann equation were solved in parallel for each layer as well as for the filament layer, while the laser photon rate equation was not used in the filament layer.

3 Simulation results and comparison with experimental data

Our final goal was to predict correctly the lasing dynamics and the laser energy as a function of the physical parameters. Therefore, it is very important to describe properly the optical characteristics of the cavity. Care was taken to adequately describe the optical losses. The absorption and reflection from the two MgF_2 windows located inside the cavity were measured and the corresponding losses were used in the model. To evaluate the role of unaccounted losses in the cavity, in Fig. 3 the dependence of the calculated laser energy on additional losses in the optical cavity is shown for an Ernst-profiled cathode for different disturbances of the electric field within a filament (δE) (marked curves) with a total filament area (S_f) of 1.1 cm^2. It is seen that additional losses of a reasonable value can not explain the difference between experimental and computed laser energy.

In Fig. 4a the measured current (J_{PFN}(exp)) and voltage (V_P(exp)) waveforms are compared with calculated ones; in Fig. 4c the measured and calculated laser pulse waveforms are compared, too. The first peak in the experimentally observed laser pulse is attributed to lasing of atomic fluorine ($\lambda = 713$ nm). Because of the high intensity it was not completely filtered out. The gain kinetics for this transition was ignored in the model because of the negligible role of this process. Figure 4b presents the calculated discharge current and voltage pulses. The presented results were calculated for a radiation absorption and scattering loss in the windows of 20% per single pass. The outcoupling mirror has a reflectance of 70%. The calculated laser energy is 158 mJ compared to 90 mJ measured in the experiment. Increasing the additional losses in the calculation up to 40% per single pass resulted in an output energy of 98 mJ, which is close to the experimental value (see Fig. 3). But in this case the calculated form of the laser pulse differs even more from the measured one. In Fig. 4d the calculated evolution of the electron number density and the F_2 concentration within a filament are shown relative to bulk density and to the initial value, respectively. It can be seen that the growth of the electron density goes ahead of the halogen depletion process. When the influence of the micro-arcs on the lasing process is ignored, both the calculated pulse length and pulse energy were higher than in the experiments. This discrepancy can not be explained by a reasonable increase of the radiation losses in the laser cavity (see Fig. 3). However, inclusion of discharge filamentation in the model yielded a reasonable agreement between experiment and theory both in the shape of the laser pulse and in its energy. As discussed above, the field disturbance (δE) in the filaments was taken as equal to 0.7%. Our model also allows us to calculate the spatial profiles of all physical quantities. The calculated dynamics of the transverse spatial distributions for the same conditions as in Fig. 4 are illustrated in Fig. 5. According to the electrode profile, a LSSN leads in the

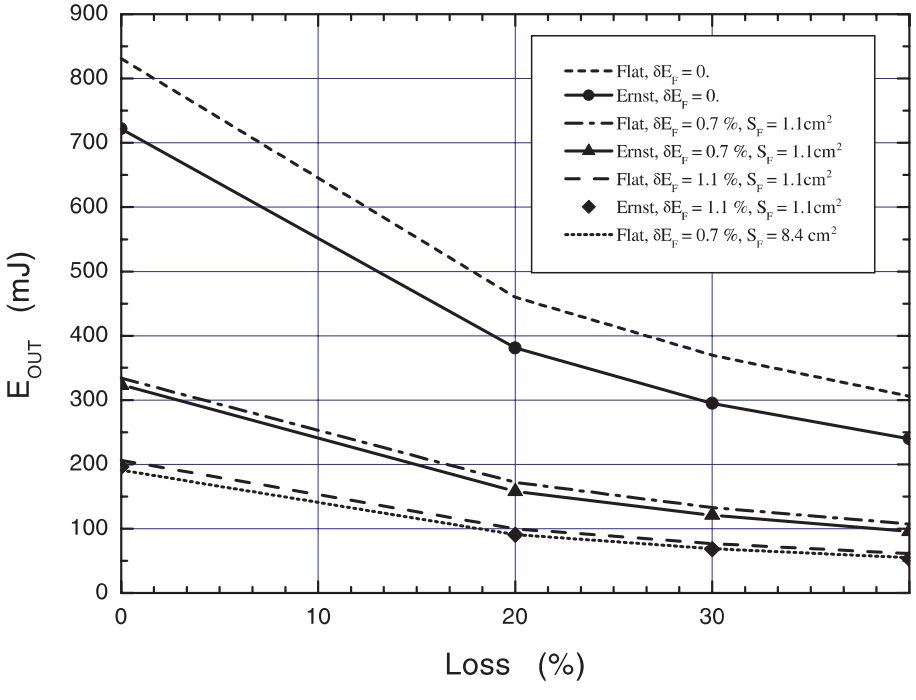

Fig. 3. Calculated laser energy as a function of the additional losses in the optical cavity for profiled (Ernst) and flat (Flat) cathodes for different values of the electric field disturbance in a filament (δE_F) and filament cross-section areas (S_F)

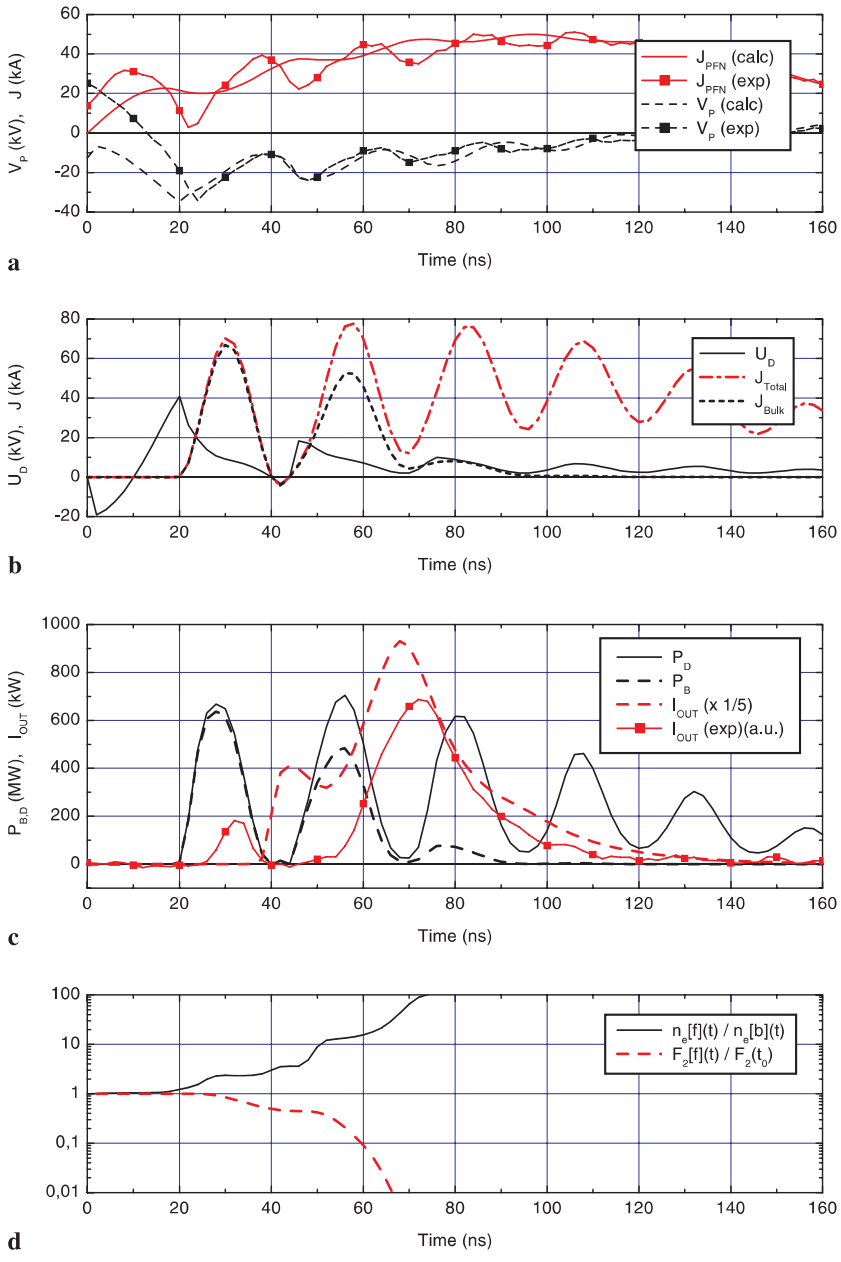

Fig. 4a–d. Time evolution of different characteristic signals. (Filament area $S_F = 1.1\,cm^2$; relative electric field fluctuation inside a filament $\delta E_F = 0.7\%$, Ernst's profile cathode.) **a** Measured current J_{PFN} and voltage V_P (see Fig. 2) compared with calculated quantities. **b** Calculated discharge voltage U_D, total discharge current J_{Total} and current in the bulk of the plasma J_{Bulk}. **c** Calculated total power dissipated in the discharge P_D, in the bulk of the plasma P_B, the calculated optical output I_{OUT} and the experimental optical output I_{EXP}. **d** The calculated electron concentration in the filament relative to the bulk of the plasma $n_e[f](t)/n_e[b](t)$, and the fluorine density in the filament reduced to the initial value $F_2[f](t)/F_2(t_0)$

centre of the discharge to an increase of the current, the input power, the electron, F, F* concentrations and the photon density. On the other side, due to depletion the F_2 concentration has a minimum and is very low at the end of the pulse here. In contrast, the concentrations of F^- and Ar* have plateaux because of the balance of the rates for creation and destruction. The laser generation takes place only in the central part of electrodes, therefore the excimer molecules have a hole in their spatial distribution. The computed time dependencies of the distribution widths for a number of physical quantities are shown in Fig. 6. The oscillations in the discharge current, theoretically predicted for these conditions (see Fig. 4), resulted in a non-monotonous behaviour of the widths of the distributions of the electric current, of the excited species densities and of the laser power. The evolution of a LSSN in the form of a constricted channel at the discharge axis for the discharge current and laser energy is clearly seen in Fig. 6a and c. It should be emphasised that the current channel eventually constricts stronger than the laser beam, resulting in a discharge width narrower than the laser beam. This is explained by the saturated dependence of the excimer molecule density on the electron number density. Note that the calculated beam width for the laser energy of 0.6 cm (see Figs. 5d and 6) agrees quite well with the experimental result of 0.7 cm.

4 Numerical parametric studies of laser characteristics

A comparison of the simulation results with experimental data carried out above shows the applicability of the model formulated for a rather complicated experimental device. To clarify the role played by different factors included in the model some parametric studies were performed numerically.

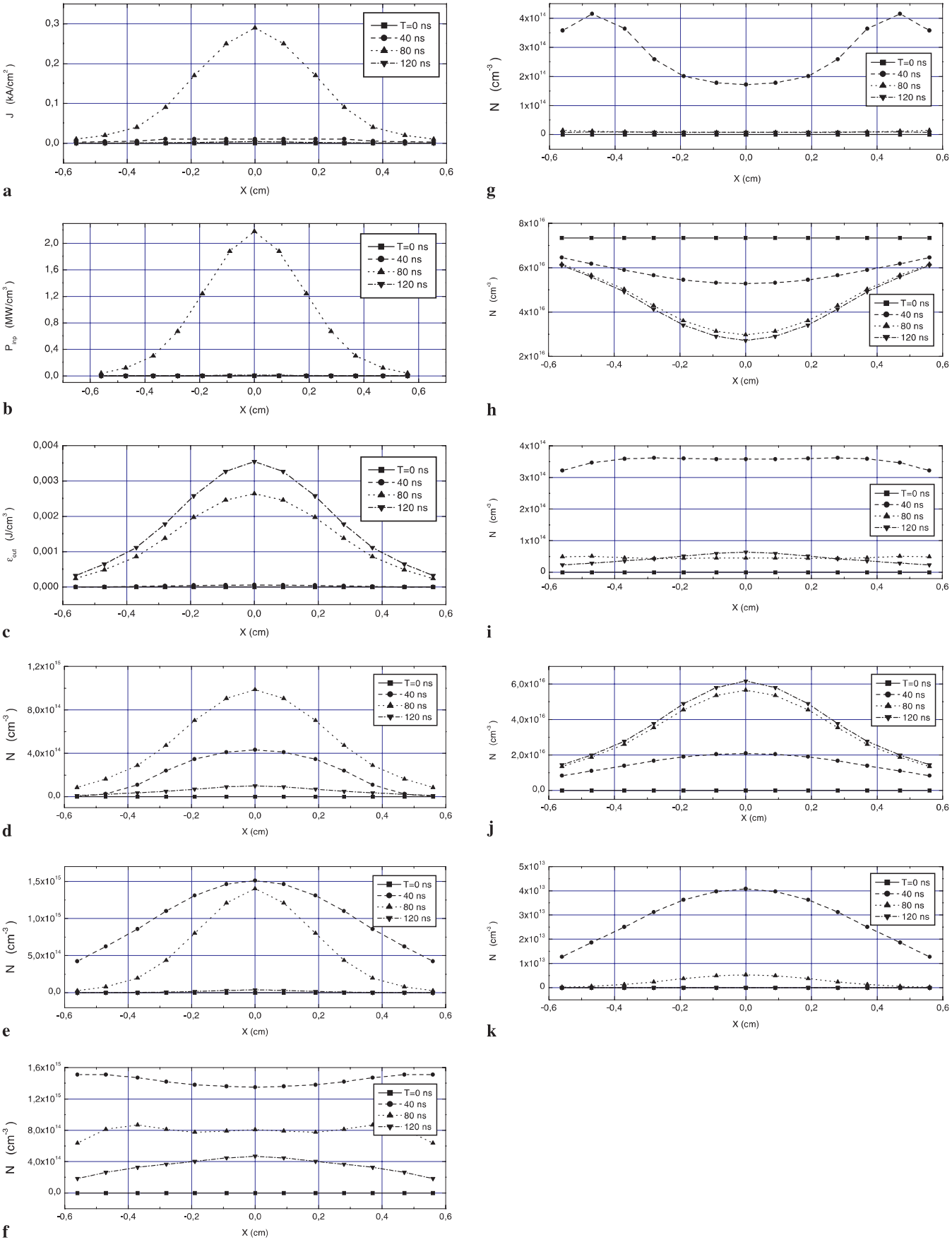

Fig. 5a–k. Temporal evolution of the spatial distribution of **a** the current, **b** the input power, **c** the output energy and **d** photon concentration and the densities of **e** electron, **f** Ar^*, **g** ArF^*, **h** F_2, **i** F^-, **j** F and **k** F^* for the same conditions as in Fig. 4

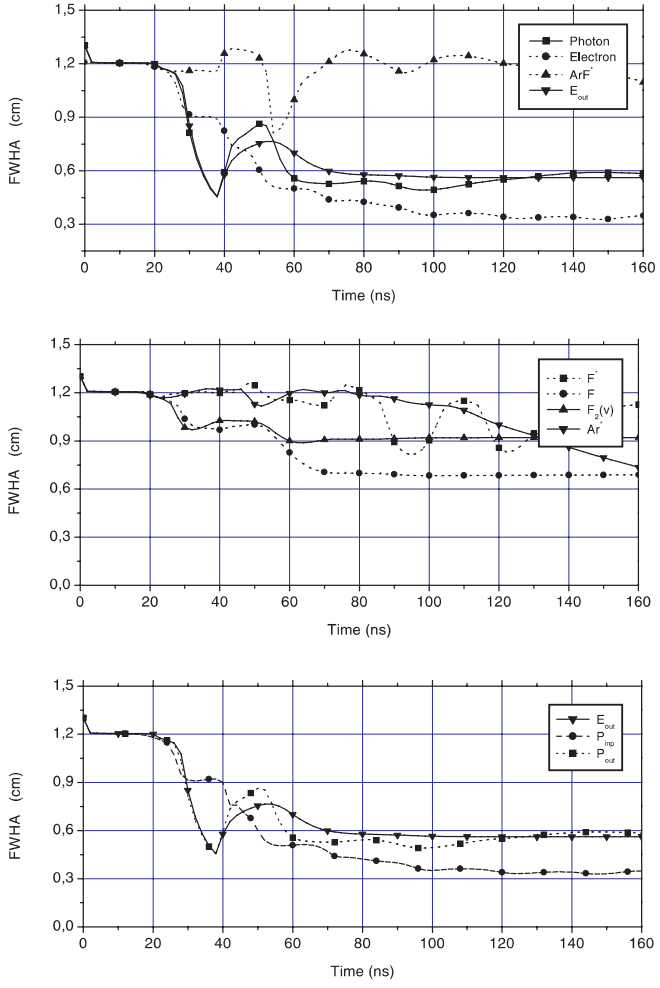

Fig. 6. Time evolution of the full-width at half-amplitude (FWHA) of the spatial distribution of different species and of the current, the input power and the output energy for the same conditions as in Fig. 4

4.1 Electrode profile and micro-arcs formation

In the experiment the cathode surface was profiled according to Ernst [24] to provide a uniform distribution of the initial electric field over the discharge volume. To estimate the role of the cathode profile a comparison was made with a cathode with a flat part in the centre. Calculations were made for these two systems. In the model the width of the flat parallel part of the cathode was taken as equal to the experimentally observed width of the laser beam of 0.7 cm. In fact, the model in this case exactly coincides with the zero-dimensional model (0-D model) in which filament formation is allowed. This model is frequently used in the literature (e.g. see [10, 15, 16]). In Fig. 3, it can be seen that for the actual cathode profile the computed energy is lower than for the flat one, provided all other conditions are kept the same. Note that the difference in output energy is lower when the development of a filament is allowed. In Fig. 7 the calculated waveforms of the total discharge power P_D, the power dissipated in the bulk of the plasma P_B and the calculated optical output I_{OUT} are compared for various parameters of the electrical circuit, with and without plasma filamentation and for different electrode profiles. Comparing Figs.4c and 7a and looking at Fig. 3, the conclusion can be drawn that the PRM with realistic electrode profiles provides a better agreement with the experiment than the 0-D model, both in the waveforms and in the laser energy. An increase of the electric field disturbance within the filaments, or of the area occupied by them, results in a laser energy getting closer to the experimental value for the flat electrodes (see Fig. 3). Agreement is achieved for a perturbation of the electrical field of 1.1% or with a micro-arc area of 8.4 cm^2. However, the calculated form of the laser pulse with its energy close to the experimental value, differs even more strongly from the measured one than those shown in Figs.7e and f.

To illustrate the role of the micro-arcs, simulations were made for the actual electrode profile while neglecting the formation of filaments. While there is no strong difference in the observed discharge current and voltage, the laser pulse is remarkably higher and longer when the instabilities are ignored (compare Figs.4 and 7b). The calculated laser pulse energy in this case is 381 mJ with additional losses of 20% (see Fig. 3).

4.2 Electrical circuit parameters

In the experimentally used electric circuit there exists a strong difference between the capacitance of the PFN and the peaking capacitor. As a result, the discharge current is modulated by oscillations associated with the circuit involving the peaking capacitor (see Fig. 4). The repetition frequency of oscillations is governed by the value of the peaking capacitance and the inductance of the local circuit, $L_P + L_{El}$. According to the calculations, if no micro-arcs evolve, six electric-discharge pulses would excite the active medium, and the output would consist of four laser peaks (see Fig. 7b). The development of micro-arcs limits lasing to two peaks (see Fig. 4 and Fig. 7a). Decreasing the inductance of the peaking capacitor should increase the discharge energy that is consumed by the lasing process. In Fig. 7c the results are presented for the ideal case of this inductance being zero. The reduction of the period between the electric-discharge pulses results in an increase of the input power, while the stability time slightly increases. The output energy increases up to 219 mJ (as compared to 158 mJ in Fig. 4). The laser pulse starts earlier and decays more smoothly. For a further illustration of the effect of a variation of the electric circuit parameters, in Fig. 7d the results of numerical simulations are shown for the same conditions as in Fig. 4 except for a doubling of both the peaking capacitance C_P and inductance L_P. In this case only the first current pulse of the pulse train results in a laser pulse. The predicted pulse energy becomes 115 mJ and the pulse shape is quite similar to the experimental waveform. However, the period of the voltage oscillations at V_P is twice as long as that of the experimentally measured waveforms.

4.3 Effects of the EEDF

A specific feature of our model is that it involves the integration of the Boltzmann equation for each layer of the plasma as well as for the filaments. In the PRM, two approaches used to be employed in the past for the treatment of the electron energy distribution function (EEDF): in the first

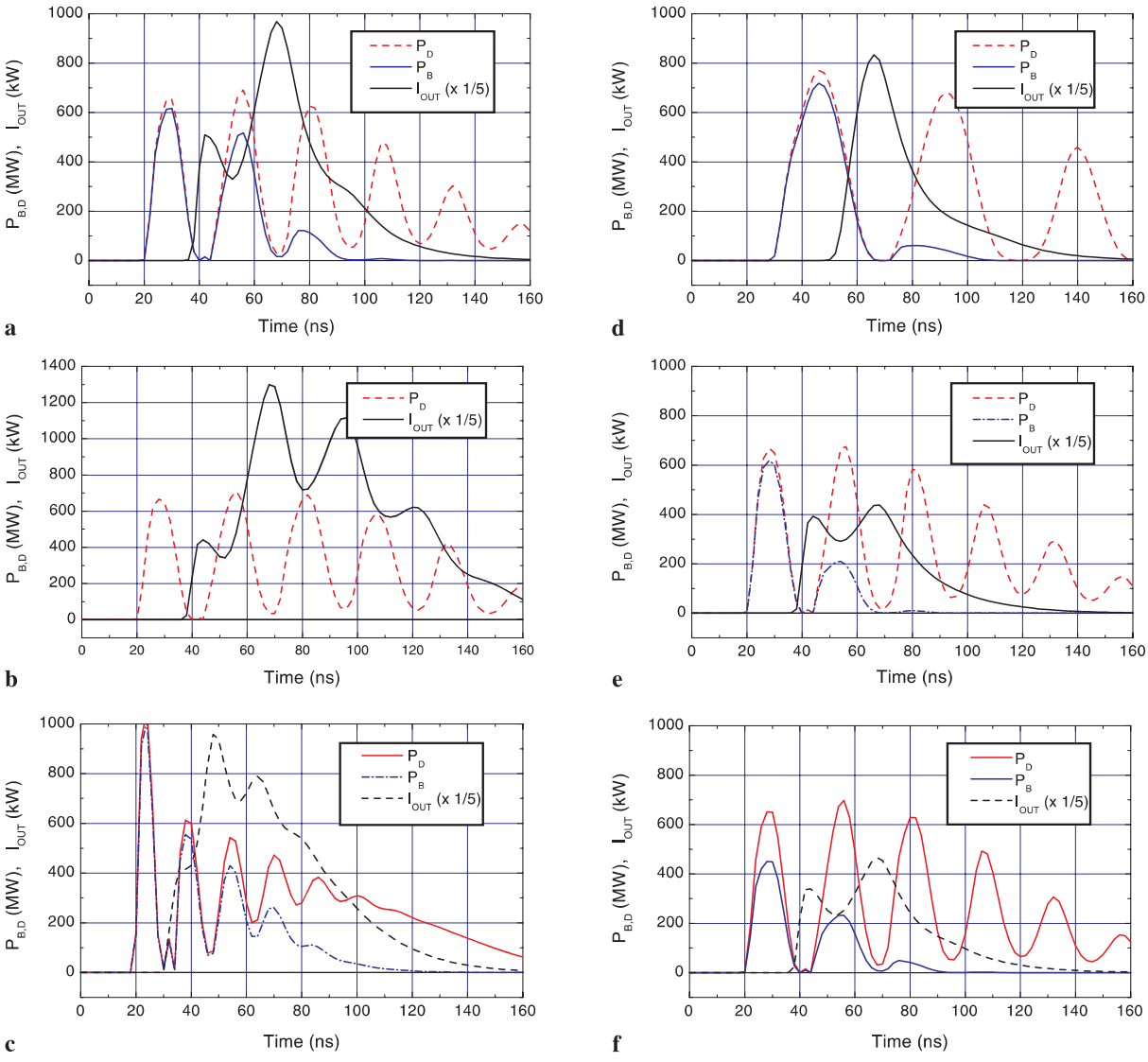

Fig. 7a–f. Calculated time evolution of total power dissipated in the discharge P_D, in the bulk of the plasma P_B and the optical output I_{OUT}, for the same conditions as in Fig. 4 except: **a** Ernst's cathode replaced by a flat cathode; **b** without plasma filamentation; **c** with self-inductance $L_P = 0$ nH; **d** with doubled self-inductance and peaking capacitance; $L'_P = 2L_P$, $C'_P = 2C_P$; **e** with $\delta E_F = 1.1\%$; **f** with Ernst's cathode replaced with a flat cathode and $S_F = 8.4\,\text{cm}^2$

one, the assumption was made that the EEDF is Maxwellian and an equation for the evolution of the electron temperature was included. In the second approach, the EEDF and all respective kinetic coefficients were calculated in advance for the 'cold' plasma, stored and then used in the calculation by interpolation of the values necessary for the integration of the kinetic equations system. As is seen from Fig. 8, neither of these assumptions is valid for the situation under consideration. The EEDF is shown calculated for three different plasma layers, positioned at the axis ($x = 0$), at $x = 2.79$ mm, and at $x = 5.58$ mm (close to the laser beam boundary), and for the filament. In the shape of the EEDF, strong deviations from the Maxwellian distribution having a form of a straight line are clearly seen. The appearance of a wavy structure, later in the discharge, can be explained by the influence of super-elastic collisions in combination with electron–electron (e–e) collisions. The discharge and laser pulses calculated with a fixed electron concentration and neglecting super-elastic collisions are remarkably longer than in Fig. 4, and no micro-arc formation is seen. Figure 9 shows a direct comparison of the laser pulse waveform for these three cases (we include also the case when the electron number density is fixed at a level of $1.75 \times 10^{12}\,\text{cm}^{-3}$), for clarity the experimental waveform is shown, too. The strong difference between the calculated waveforms is evident, and it is attributed completely to the development of instabilities associated with the deformation of the EEDF. It is seen also that super-elastic collisions play an insignificant role in this effect. It should be noted that the so-called mechanism of halogen depletion instability, widely discussed in the literature (for example in [17]), is included in our model. However, under our conditions it plays a minor role, if any. The most striking illustration of the importance of a correct modelling with respect to the e–e and super-elastic collisions is the fact that in the case when the e–e and super-elastic collisions are neglected in the calculations, the Boltzmann equation theory predicts that at the applied voltage no high-current discharge exists. For the given parameters of the specific electric cir-

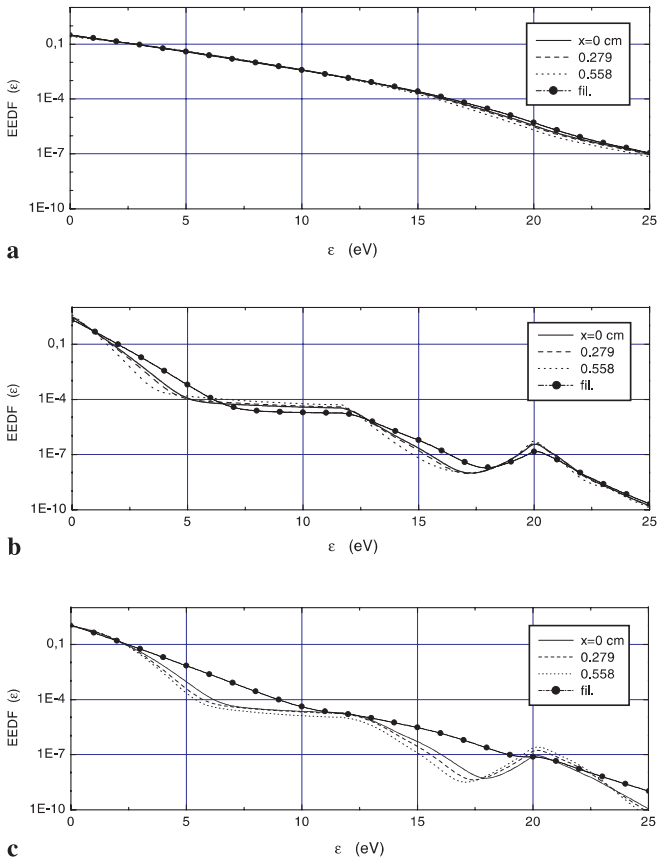

Fig. 8a–c. EEDF at several positions in the bulk plasma ($x = 0$; 0.279; 0.558 cm) and in the filament for time **a** 30 ns, **b** 40 ns and **c** 100 ns for the same conditions as in Fig. 4

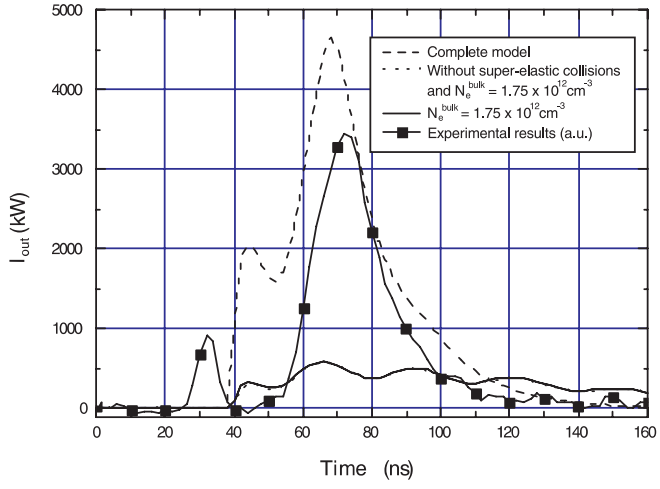

Fig. 9. Comparison between the experimental and the calculated laser pulse waveforms for different approximations of the electron kinetics. *Dashed line:* complete model for the situation in Fig. 4. *Solid line:* Boltzmann equation computed with a fixed electron concentration of $n_e = 1.75 \times 10^{12}\,\mathrm{cm}^{-3}$ and neglecting second-order collisions. *Short-dashed line:* Boltzmann equation computed with a fixed electron concentration of $n_e = 1.75 \times 10^{12}\,\mathrm{cm}^{-3}$. *Solid line and symbol:* experimental result

cuit and applied voltage, the discharge-current waveform appears to be rather sensitive to small variations in the shape of the EEDF. Inclusion of the e–e collisions at an electron concentration as low as $1.75 \times 10^{12}\,\mathrm{cm}^{-3}$ results in the development of a high-current peak, while with no e–e collisions the balance between the ionisation and attachment processes became negative. For an electron concentration in the plasma higher than $10^{15}\,\mathrm{cm}^{-3}$, the role of e–e collisions is much more important, resulting in a rapid development of instabilities.

5 Conclusions

A rather good agreement is achieved between the discharge and laser characteristics, predicted by a PRM including the formation of filaments and the experimental results on a self-sustained discharge-excited ArF laser. It is shown that the inclusion in the model of the formation of micro-arcs, followed by a redistribution of the current between the bulk of the plasma and the filament array is of crucial importance to the model. The assumption was made that the electric power dissipated in the filaments was lost for the lasing process. It is shown that it is important to properly include in the model a description of the electrode profile and to calculate the Boltzmann equation for the electron energy distribution function for each layer as well as for the filaments. In particular, known mechanisms for discharge instabilities, such as step-wise ionisation and halogen depletion, taken solely cannot explain the observed stability time. It turned out that only a combination of these mechanisms together with a deformation of the EEDF, induced by electron–electron and second-kind collisions, can satisfactorily explain the experimental data. A strong difference between the predictions by a 0-D model and the present 1-D model is demonstrated. The developed model describes the evolution of the transverse profiles for the discharge current, the laser power and the distributions of various species. A surprising result from the model is that the spatial width of the calculated current distribution is less than that of the optical beam. Modelling showed the possibility of controlling the characteristics of the laser by varying some parameters of the electric circuit. Recommendations are given for the electric circuit parameters.

Acknowledgements. The present work has been supported by the Netherlands Technology Foundation STW and by the Netherlands Foundation for Scientific Research NWO.

References

1. S. Nagai, H. Furuhashi, A. Kono, Y. Uchida, T. Goto: IEEE J. Quant. Electron. **34**, 942 (1998)
2. S. Nagai, H. Furuhashi, A. Kono, T. Goto, Y. Uchida: IEEE J. Quant. Electron. **34**, 40 (1998)
3. S. Nagai, H. Furuhashi, Y. Uchida, J. Yamada, A. Kono, T. Goto: J. Appl. Phys. **77**, 2906 (1995)
4. V.M. Borisov, I.E. Bragin, A.Y. Vinokhodov, V.A. Vodchits: Sov. J. Quantum Electron. **25**, 507 (1995) [Kvantovaya Elektron. **22**, 533 (1995)]
5. A.A. Zhupikov, A.M. Razhev: Sov. J. Quantum Electron. **27**, 665 (1997)
6. L. Feenstra, H.M.J. Bastiaens, P.J.M. Peters. W.J. Witteman: Appl. Phys. Lett. **75**, 1033 (1999)
7. T. Saito, S. Ito, A. Tada: Appl. Phys. B **63**, 229 (1996)
8. S. Ito, T. Saito, A. Tada: Rev. Sci. Instrum. **67**, 658 (1996)
9. T. Saito, S. Ito: Appl. Phys. B **66**, 579 (1998)
10. D. Lo, A.I. Shchedrin, A.V. Ryabtsev: J. Phys. D **29**, 43 (1996)
11. H. Akashi, Y. Sakai, H. Tagashira: J. Phys. D **27**, 1097 (1994)
12. H. Akashi, Y. Sakai, H. Tagashira: J. Phys. D **28**, 445 (1995)

13. H. Akashi, Y. Sakai, H. Tagashira: Austr. J. Phys. **50**, 655 (1997)
14. R.S. Taylor: Appl. Phys. B **41**, 1 (1988)
15. N.S. Belokrinitskii, V.N. Gorshkov, A.I. Shchedrin: Zh. Tekh. Fiz. **63**, 81 (1993) [Tech. Phys. **38**, 409 (1993)]
16. M.J. Kushner, A.L. Pindroh, C.H. Fisher, T.A. Znotins, J.J. Ewing: J. Appl. Phys. **57**, 101 (1987)
17. M.J. Kushner: IEEE Trans. Plasma Sci. **19**, 387 (1991)
18. I.O. Blinov, A.V. Dem'yanov, A.V. Kochetov, A.P. Napartovich, A.P. Pastor, P.Y. Serdobintsev, N.N. Shubin: Kvantovaya Electron. **15**, 2441 (1988) [Sov. J. Quantum Electron. **18**, 1531 (1988)]
19. R.J. Sorkina: J. Phys. D **23**, 806 (1990)
20. S. Longo, G. Comunale, C. Gorse, M. Capitelli: Plasma Chem. Plasma Process. **13**, 685 (1993)
21. A.V. Dem'yanov, I.V. Kochetov, A.P. Napartovich, S. Longo, M. Capitelli: Plasma Chem. and Plasma Proc. **16**, 121 (1996)
22. V.M. Borisov, O.B. Khristoforov, Y.B. Kirykhin, A.Y. Vinokhodov, A.I. Demin, A.V. Dem'yanov: Proc. SPIE **2987**, 94 (1997
23. S. Gorchakov, D. Lofgagen, R. Winkler: Appl. Phys. B **66**, 313 (1998)
24. G.J. Ernst: Opt. Commun. **49**, 275 (1984)
25. S.J. Scott: Appl. Phys. B **56**, 201 (1993)
26. F.A. van Goor: J. Phys. D **26**, 404 (1993)
27. L. Feenstra, O.B. Hoekstra, P.J.M. Peters, W.J. Witteman: Proc. SPIE **3574**, 67 (1998)
28. W.H. Long, M.J. Plummer, E.A. Stappaerts: Appl. Phys. Lett. **43**, 735 (1983)
29. E.C. Beaty, P.L. Petterson: Phys. Rev. **137**, A364 (1965)
30. D. Smith, P.R. Cromey: J. Phys. B **1**, 638 (1968)
31. D.K. Bohme, D.B. Dunkin, F.C. Fehsenfeld, E.E. Ferguson: J. Chem. Phys. **51**, 863 (1969)
32. J.H. Kolts, D.W. Setser: J. Phys. Chem. **82**, 1766 (1978)
33. Calculated for a pressure of 5 bar, using the formulas of M.R. Flannery, T.P. Yang: Appl. Phys. Lett. **32**, 356 (1978)
34. J.W. Keto, C.Y. Kuo: J. Chem. Phys. **74**, 6188 (1981)
35. M. Ohwa, M. Obara: J. Appl. Phys. **63**, 1306 (1988)
36. A.M. Boichenko, V.I. Derzhiev, S.I. Yakovlenko: Laser Phys. **2**, 210 (1992)
37. *Excimer Lasers*, ed. by C.K. Rodes (Springer, Berlin, Heidelberg, New York 1979)
38. M. Hayashi, T. Nimura: J. Appl. Phys. **54**, 4880 (1983)
39. A.V. Hazi, A.E. Orel, T.N. Resigno: Phys. Rev. Lett. **46**, 918 (1981)
40. J.L. Pack: J. Appl. Phys. **71**, 5363 (1992)
41. A.J. Dixon, M.F.A. Harrison, A.C.H. Smith: J. Phys. B **9**, 1267 (1976)